

Parallel imaging in time-of-flight magnetic resonance angiography using deep multistream convolutional neural networks

Yohan Jun¹  | Taejoon Eo¹ | Hyungseob Shin¹ | Taeseong Kim¹ |
Ho-Joon Lee^{2,3}  | Dosik Hwang¹

¹School of Electrical and Electronic Engineering, Yonsei University, Seoul, Korea

²Department of Radiology and Research Institute of Radiological Science, Severance Hospital, Yonsei University College of Medicine, Seoul, Republic of Korea

³Department of Radiology, Inje University College of Medicine, Haeundae Paik Hospital, Busan, Republic of Korea

Correspondence

Dosik Hwang, College of Engineering,
Yonsei University, 50 Yonsei-ro,
Seodaemun-gu, Seoul, 03722, Korea.
Email: dosik.hwang@yonsei.ac.kr

Funding information

National Research Foundation of Korea (NRF) grant funded by the Korean government (MSIP; 2016R1A2B4015016) and National Research Foundation of Korea (NRF) grant funded by the Korean government (MSIT; 2018M3C7A1024734)

Purpose: To develop and evaluate a method of parallel imaging time-of-flight (TOF) MRA using deep multistream convolutional neural networks (CNNs).

Methods: A deep parallel imaging network (“DPI-net”) was developed to reconstruct 3D multichannel MRA from undersampled data. It comprises 2 deep-learning networks: a network of multistream CNNs for extracting feature maps of multichannel images and a network of reconstruction CNNs for reconstructing images from the multistream network output feature maps. The images were evaluated using normalized root mean square error (NRMSE), peak signal-to-noise ratio (PSNR), and structural similarity (SSIM) values, and the visibility of blood vessels was assessed by measuring the vessel sharpness of middle and posterior cerebral arteries on axial maximum intensity projection (MIP) images. Vessel sharpness was compared using paired *t* tests, between DPI-net, 2 conventional parallel imaging methods (SAKE and ESPIRiT), and a deep-learning method (U-net).

Results: DPI-net showed superior performance in reconstructing vessel signals in both axial slices and MIP images for all reduction factors. This was supported by the quantitative metrics, with DPI-net showing the lowest NRMSE, the highest PSNR and SSIM (except $R = 3.8$ on sagittal MIP images, and $R = 5.7$ on axial slices and sagittal MIP images), and significantly higher vessel sharpness values than the other methods.

Conclusion: DPI-net was effective in reconstructing 3D TOF MRA from highly undersampled multichannel MR data, achieving superior performance, both quantitatively and qualitatively, over conventional parallel imaging and other deep-learning methods.

KEYWORDS

deep-learning, magnetic resonance angiography, multistream network, parallel imaging, time-of-flight

1 | INTRODUCTION

Blood flow in the human body can be visualized noninvasively using MRA, based on the moving spin effects of the MR signals.¹ A commonly used non-contrast-enhanced technique for this is 3D time-of-flight (TOF) MRA, which is used to diagnose vascular-related diseases such as intracranial vascular aneurysms, stenosis, and occlusion.²⁻⁷ However, 3D TOF sequences inevitably require an increased scan time to cover the large field of view and to provide detailed vascular anatomy information with high spatial resolution, and this potentially increases the risk of motion-related artifacts.⁸

To reduce MRI scan times, k-space data can be undersampled during the scan. However, undersampling below the Nyquist sampling rate in the frequency domain results in aliasing artifacts in the spatial domain. Several methods have been proposed to solve this problem, one of which is an algorithm based on compressed sensing MRI.^{9,10} This algorithm reconstructs undersampled MR images through l_1 minimization using the property of sparsity when transforming an MR image into a specific domain (such as a wavelet or a discrete cosine transform). Recent studies have demonstrated the clinical feasibility of fast TOF MRA using a compressed sensing-based iterative method.^{11,12}

Other fast MRI methods include those based on parallel imaging (PI). These remove the aliasing artifacts in the image domain attributed to undersampling in k-space in 3 ways, by: (1) using the sensitivity map information of the receiver coils in the image domain; (2) filling empty k-space lines using the autocalibration signal information of the k-space; or (3) using low-rank matrix completion without the autocalibration signal information.¹³⁻¹⁶ These methods allow the effective reconstruction of MR images from undersampled k-space data obtained from multiple receiver coils, but they require considerable reconstruction time, especially when applied to 3D MR images.¹⁷ For example, it can take several hours for PI reconstruction for large MR data sets such as for multichannel 3D TOF MRA, so the method is not feasible for online reconstruction, which must be completed in only a few minutes.^{15,17} Furthermore, the high reduction factor of PI MRA is still limited by the decrease in signal-to-noise ratio (SNR).^{8,11}

In recent years, various deep-learning-based methods have been proposed, with convolutional neural networks (CNNs), an architecture widely used in deep-learning, outperforming conventional image processing algorithms in image super-resolution, denoising, and inpainting.¹⁸⁻²¹ Several studies have applied deep-learning to processing medical images, especially for MR image reconstruction from undersampled k-space data, demonstrating better performance than with the conventional compressed sensing or PI-based methods even when the reduction factor was high.²²⁻²⁶

However, there may be limitations to applying conventional deep-learning-based methods to accelerate 3D TOF

MRA. Several methods have been proposed for reconstructing MR images from undersampled 2D k-space data. For example, undersampled 2D multichannel MR images have been reconstructed by line-by-line (1D vector) in the phase encoding direction using a multilayer perceptron²³ or using a variational network.²⁴ Given that 3D TOF MRA has high spatial resolution and vessel signals are connected within adjacent slices, it is reasonable to reconstruct vessel signals from undersampled 3D MR data using the deep-learning-based method, which can learn to reconstruct 3D MR structures. To the best of our knowledge, there have been no previous studies of reconstructing 3D MR images from undersampled 3D k-space data acquired from 3D TOF MRA sequences using deep-learning-based methods. We have therefore developed a 3D PI method based on 3D CNNs to reconstruct undersampled 3D TOF MRA data acquired from multiple channels.

In addition, conventional methods do not use multichannel information effectively to reconstruct MR images acquired from multiple channels each with different coil sensitivity characteristics. In conventional deep-learning-based methods, undersampled multichannel MR images have been fed together as input into 1 neural network, so that information from the channels is mixed regardless of the characteristics of each channel.²³ Recent studies have proposed that data with multiple channel information, such as multiframe videos or RGB data with depth image, should be addressed with multistream CNNs to improve performance.^{27,28} In the present study, multistream CNNs architecture was introduced to address MR images acquired from multiple channels. Each channel's undersampled MR image was fed in parallel as input into the multistream CNNs and output feature maps were obtained. Then, reconstruction CNNs processed the feature maps, and the final MR image was reconstructed from the output of the reconstruction CNNs.

In summary, we have developed a 3D PI method (called "DPI-net"; abbreviated from Deep Parallel Imaging Network) that reconstructs 3D TOF MRA from undersampled multichannel MR data using CNNs. It comprises 2 deep-learning networks: a network of multistream CNNs (MS-net) for extracting the feature maps of multichannel images and a network of reconstruction CNNs (RC-net) for reconstructing images from the MS-net output feature maps. In this study, we describe DPI-net and evaluate its effectiveness in reconstructing 3D TOF MRA in comparison with existing methods.

2 | METHODS

2.1 | Problem formulation

The fully sampled 3D MR image of the c -th coil ($c = 1, \dots, N_c$) with a sensitivity map can be expressed as follows (Equation 1):

$$\mathbf{I}_f^c = \mathbf{I}_f \circ \mathbf{S}^c, \quad (1)$$

where $\mathbf{I}_f^c \in \mathbb{C}^{N_{k_x} \times N_{k_y} \times N_{k_z}}$ is the fully sampled image of the c -th coil, $\mathbf{S}^c \in \mathbb{R}^{N_{k_x} \times N_{k_y} \times N_{k_z}}$ is the sensitivity map of that coil, and \circ denotes elementwise multiplication. The undersampled k-space and image for the c -th coil can then be expressed as follows (Equations 2 and 3):

$$\mathbf{k}_u^c = \mathbf{U}_m \circ \mathcal{F}_{3D}(\mathbf{I}_f^c) \quad (2)$$

$$\mathbf{I}_u^c = \mathcal{F}_{3D}^{-1}(\mathbf{k}_u^c), \quad (3)$$

where $\mathbf{k}_u^c \in \mathbb{C}^{N_{k_x} \times N_{k_y} \times N_{k_z}}$ is the undersampled k-space of the c -th coil, $\mathbf{U}_m \in \mathbb{R}^{N_{k_x} \times N_{k_y} \times N_{k_z}}$ is the binary undersampling mask, \mathcal{F}_{3D} and \mathcal{F}_{3D}^{-1} are the 3D Fourier transform and inverse Fourier transform, respectively, and $\mathbf{I}_u^c \in \mathbb{C}^{N_{k_x} \times N_{k_y} \times N_{k_z}}$ is the undersampled image of the c -th coil. Our purpose was to restore the undersampled multichannel 3D MR images to a fully sampled 3D MR image using deep-learning networks. Thus, the objective function can be formulated as the following minimization equation (Equation 4):

$$\begin{aligned} & \arg \min_{\theta} \|\mathbf{y} - D_H(\mathbf{x}; \theta)\|_2^2 \\ & = \arg \min_{\theta} \left\| \sqrt{\sum_{c=1}^{N_c} |\mathbf{I}_f^c|^2} - D_H\left(\left[|\mathbf{I}_u^1|, |\mathbf{I}_u^2|, \dots, |\mathbf{I}_u^{N_c}|\right]; \theta\right) \right\|_2^2, \end{aligned} \quad (4)$$

where $\mathbf{y} = \sqrt{\sum_{c=1}^{N_c} |\mathbf{I}_f^c|^2} \in \mathbb{R}^{N_{k_x} \times N_{k_y} \times N_{k_z}}$ is the desired output (the square root of sum-of-squares [SSOS] of the fully sampled multichannel 3D MR images), $\mathbf{x} = \left[|\mathbf{I}_u^1|, |\mathbf{I}_u^2|, \dots, |\mathbf{I}_u^{N_c}|\right] \in \mathbb{R}^{N_{k_x} \times N_{k_y} \times N_{k_z} \times N_c}$ is the magnitude of the undersampled multichannel 3D MR images, and D_H is the hypothesis function of the deep-learning network with parameters θ . The objective was to find θ in Equation 4 that minimized the l_2 difference between \mathbf{y} and $D_H(\mathbf{x}; \theta)$ for the given training data set.

2.2 | Deep-learning architecture

DPI-net's deep-learning architecture is based on fully CNNs and consists of 2 main networks: MS-net, comprising multistream CNNs for extracting feature maps of multichannel images, and RC-net, comprising deep reconstruction CNNs for reconstructing the images. The overall architecture is presented in Figure 1. In this section, we introduce the forward-pass equations for each main network.

2.2.1 | MS-net: feature map extraction

MS-net has an architecture of multistream CNNs for processing each channel image. Its forward-pass equations can be represented as follows (Equations 5 and 6):

$$\mathbf{M}_1^c = \sigma\left(\varphi\left(\mathbf{w}_{M_1}^c * |\mathbf{I}_u^c| + \mathbf{b}_{M_1}^c\right)\right) \quad (5)$$

$$\mathbf{M}_n^c = \sigma\left(\varphi\left(\mathbf{w}_{M_n}^c * \mathbf{M}_{n-1}^c + \mathbf{b}_{M_n}^c\right)\right), \quad (6)$$

where $\mathbf{M}_1^c \in \mathbb{R}^{N_{k_x} \times N_{k_y} \times N_{k_z} \times c_{MS}}$, $\mathbf{w}_{M_1}^c \in \mathbb{R}^{w_{MS} \times h_{MS} \times d_{MS} \times c_{MS}}$, and $\mathbf{b}_{M_1}^c \in \mathbb{R}^{c_{MS}}$ are the output, convolution weights, and bias of the first layer of MS-net, respectively, for an input of $|\mathbf{I}_u^c|$; $*$, φ , and σ denote the convolution operation, batch normalization, and nonlinear activation function, respectively; $\mathbf{M}_n^c \in \mathbb{R}^{N_{k_x} \times N_{k_y} \times N_{k_z} \times c_{MS}}$, $\mathbf{w}_{M_n}^c \in \mathbb{R}^{w_{MS} \times h_{MS} \times d_{MS} \times c_{MS}}$, and $\mathbf{b}_{M_n}^c \in \mathbb{R}^{c_{MS}}$ are the output, convolution weights, and bias of the n -th layer of MS-net, respectively, for the input $\mathbf{M}_{n-1}^c \in \mathbb{R}^{N_{k_x} \times N_{k_y} \times N_{k_z} \times c_{MS}}$, which is the output of the previous, that is, $(n-1)$ th layer; and $n = 2, \dots, N_{L,MS}$ is the number of layers in MS-net.

The final output of MS-net is the concatenation of the $N_{L,MS}$ -th outputs, $\mathbf{M}_{N_{L,MS}}^c \in \mathbb{R}^{N_{k_x} \times N_{k_y} \times N_{k_z}}$, of each MS-net layer, represented as follows (Equation 7):

$$\mathbf{M} = \left[\mathbf{M}_{N_{L,MS}}^1, \mathbf{M}_{N_{L,MS}}^2, \dots, \mathbf{M}_{N_{L,MS}}^{N_c}\right], \quad (7)$$

where $\mathbf{M} \in \mathbb{R}^{N_{k_x} \times N_{k_y} \times N_{k_z} \times N_c}$ is the MS-net output feature maps. Thus, using multistream CNNs, we can extract the feature maps \mathbf{M} of multichannel MR images.

2.2.2 | RC-net: reconstructing the images

RC-net receives \mathbf{M} , the output feature maps of MS-net, as its input. The forward-pass equations of RC-net can be represented as follows (Equations 8 and 9):

$$\mathbf{R}_1 = \sigma\left(\varphi\left(\mathbf{w}_{R_1} * \mathbf{M} + \mathbf{b}_{R_1}\right)\right) \quad (8)$$

$$\mathbf{R}_n = \sigma\left(\varphi\left(\mathbf{w}_{R_n} * \mathbf{R}_{n-1} + \mathbf{b}_{R_n}\right)\right), \quad (9)$$

where $\mathbf{R}_1 \in \mathbb{R}^{N_{k_x} \times N_{k_y} \times N_{k_z} \times c_{RC}}$, $\mathbf{w}_{R_1} \in \mathbb{R}^{w_{RC} \times h_{RC} \times d_{RC} \times c_{RC}}$, and $\mathbf{b}_{R_1} \in \mathbb{R}^{c_{RC}}$ are the output, convolution weights, and bias of the first layer of RC-net for input \mathbf{M} ; $\mathbf{R}_n \in \mathbb{R}^{N_{k_x} \times N_{k_y} \times N_{k_z} \times c_{RC}}$, $\mathbf{w}_{R_n} \in \mathbb{R}^{w_{RC} \times h_{RC} \times d_{RC} \times c_{RC}}$, and $\mathbf{b}_{R_n} \in \mathbb{R}^{c_{RC}}$ are the output, convolution weights, and bias of the n -th layer of RC-net for input $\mathbf{R}_{n-1} \in \mathbb{R}^{N_{k_x} \times N_{k_y} \times N_{k_z} \times c_{RC}}$, that is, the output of previous, that is, $(n-1)$ th layer; and $n = 2, \dots, N_{L,RC}$ is the number of layers in RC-net.

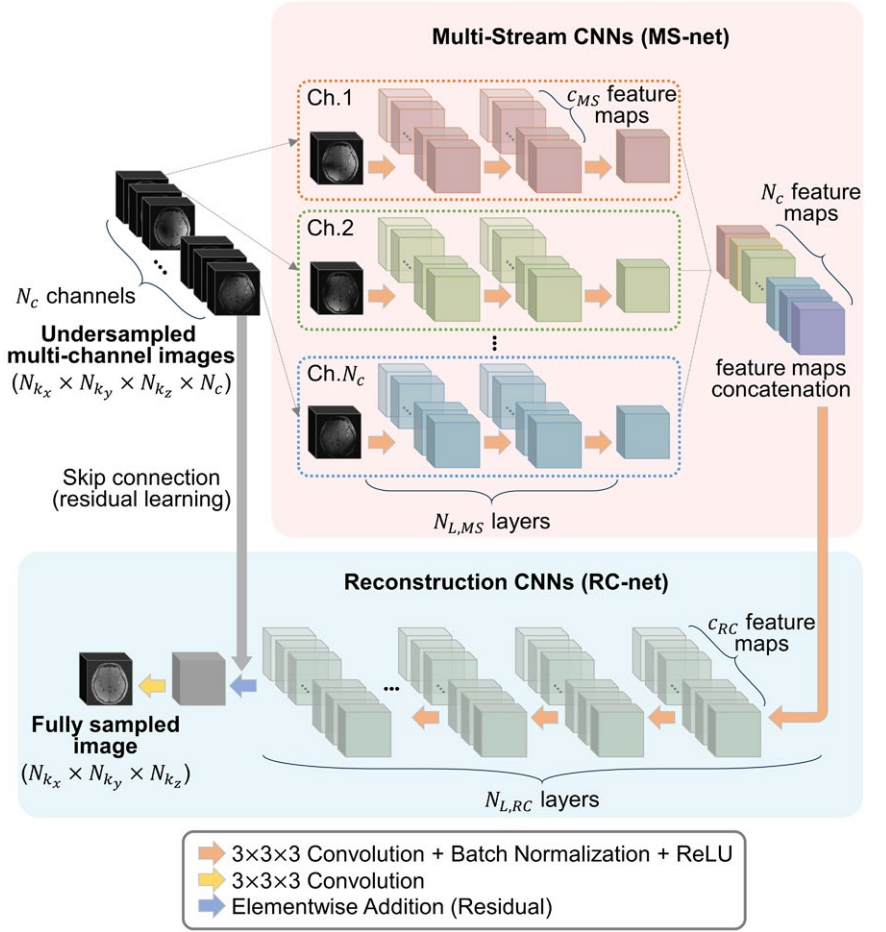


FIGURE 1 DPI-net's deep-learning architecture. This comprises 2 networks: MS-net, a network of multistream CNNs; and RC-net, a network of reconstruction CNNs. MS-net extracts the feature maps of multichannel images and RC-net reconstructs images from the MS-net output feature maps

The refinement learning (residual learning) is used by a skip connection of the input to the output of RC-net's final layer, which prevents the problem of degradation attributed to increasing the network depth and enables faster training of the CNNs.^{20,22,29} The equation can be represented as follows (Equation 10):

$$\hat{\mathbf{R}} = \mathbf{R}_{N_{L,RC}} + \mathbf{x}, \quad (10)$$

where $\hat{\mathbf{R}} \in \mathbb{R}^{N_{k_x} \times N_{k_y} \times N_{k_z} \times N_c}$ is the result of the element-wise summation of MS-net's input \mathbf{x} with the output of the $N_{L,RC}$ -th layer of RC-net, $\mathbf{R}_{N_{L,RC}} \in \mathbb{R}^{N_{k_x} \times N_{k_y} \times N_{k_z} \times N_c}$.

The final output $\hat{\mathbf{x}} \in \mathbb{R}^{N_{k_x} \times N_{k_y} \times N_{k_z}}$ is obtained by feeding the output $\hat{\mathbf{R}}$ from the refinement learning to the final convolution layer. It can be represented as follows (Equation 11):

$$D(\mathbf{x}; \boldsymbol{\theta}) = \hat{\mathbf{x}} = \mathbf{w}_F * \hat{\mathbf{R}} + \mathbf{b}_F, \quad (11)$$

where $\mathbf{w}_F \in \mathbb{R}^{w_{RC} \times h_{RC} \times d_{RC}}$ and $\mathbf{b}_F \in \mathbb{R}^1$ are the convolution weights and bias of the final convolution layer. Then $\boldsymbol{\theta}$, the parameters of the MS-net and RC-net, can be represented as follows (Equation 12):

$$\boldsymbol{\theta} = \{\boldsymbol{\theta}_M, \boldsymbol{\theta}_R\}$$

$$= \left\{ \left\{ (\mathbf{w}_{M_1}^1, \mathbf{b}_{M_1}^1), \dots, (\mathbf{w}_{M_{L_{MS}}}^c, \mathbf{b}_{M_{L_{MS}}}^c) \right\}, \left\{ (\mathbf{w}_{R_1}, \mathbf{b}_{R_1}), \dots, (\mathbf{w}_{R_{L_{RC}}}, \mathbf{b}_{R_{L_{RC}}}), (\mathbf{w}_F, \mathbf{b}_F) \right\} \right\}, \quad (12)$$

where $\boldsymbol{\theta}_M$ and $\boldsymbol{\theta}_R$ are the parameters of MS-net and RC-net, respectively.

2.2.3 | Implementation details

We implemented and trained our DPI-net in an end-to-end fashion, such that undersampled 3D multichannel MR images $\mathbf{x} = \left[\left| \mathbf{I}_u^1 \right|, \left| \mathbf{I}_u^2 \right|, \dots, \left| \mathbf{I}_u^c \right| \right]$ were fed into the MS-net and then the reconstructed 3D SSOS MR image $\hat{\mathbf{x}}$ was obtained as the output of RC-net.

MS-net consists of 3 layers ($N_{L,MS} = 3$): 2 3D convolution layers with batch normalization (φ)³⁰ and rectified linear unit (ReLU) activation function (σ),³¹ and a final layer with only one 3D convolution layer. The kernel size of all the convolution layers in MS-net is $3 \times 3 \times 3$ (i.e., $w_{MS} = h_{MS} = d_{MS} = 3$). The number of feature maps of the first 2 convolution layers is $c_{MS} = 8$ and that of the final convolution layer is 1. RC-net consists of 16 layers, including the final convolution layer: fifteen 3D convolution layers (i.e., $N_{L,RC} = 15$) with batch

normalization and ReLU activation function, and a final layer with only one 3D convolution layer. The kernel size of all the convolution layers in RC-net is also $3 \times 3 \times 3$ (i.e., $w_{RC} = h_{RC} = d_{RC} = 3$). The number of feature maps of the 15 convolution layers is $c_{RC} = 32$ and that of the final convolution layer is 1.

The input of each convolution layer was zero-padded by 1 pixel in each dimension to maintain the size of the images. All convolution weights were initialized with MSRA initialization, which prevents the vanishing gradient problem in deep neural networks.³² Another regularizer that we used to prevent the vanishing gradient problem is batch normalization.³⁰ Batch normalization is applied to each convolution layer except the final layer of RC-net. We used Adam optimizer³³ with an initial learning rate 1×10^{-4} , which was reduced to 0.5×10^{-4} after 200 epochs. DPI-net was trained with 400 epochs; this took approximately 48 hours using an Intel i7-6700K central processing unit (CPU) with an Nvidia GeForce GTX 1080Ti graphics processing unit (GPU) and 32-GB random access memory (RAM), implemented using the python *Tensorflow* library.³⁴

2.3 | Image acquisition

We acquired in vivo data from our local institution. All experiments conducted in this study were approved by the institutional review board, and written informed consent was obtained from all the human subjects. MRI was performed using a 3.0T scanner (Ingenia CX; Philips Medical Systems, Best, The Netherlands) with a 32-channel sensitivity-encoding head coil. Data for 7 subjects were acquired using 3D TOF sequences, with 3 subjects' data sets used for the training set, 3 for the test set, and 1 for the validation set. The parameters of 3D TOF sequence were as follows: TR, 20 ms; TE, 3 ms; flip angle, 18° ; matrix size, 432×432 ; pixel resolution, $0.49 \times 0.49 \text{ mm}^2$; slice thickness, 0.5 mm; and acquisition time, 11 minutes 51 seconds. Three slabs were acquired using 3D TOF sequences, each with 56 slices. A total of 120 slices were reconstructed from the 3 slabs, with the matrix size of the 3D volume image being $432 \times 432 \times 120$.

2.4 | Data preprocessing

We retrospectively undersampled 3D TOF MRA k-space data for each slab with a variable-density Poisson-disk sampling pattern^{16,35} on (k_y, k_z) domain such that the k-space data were fully sampled in the readout direction (k_x). The reduction factors were $R = 3.8, 5.7, \text{ and } 7.6$; their sampling patterns are presented in Supporting Information Figure S1. The volume images were normalized according to the maximum value of the whole 3D multichannel volume images; the pixel intensities of the magnitude image were therefore bounded between 0 and 1. For the training of the deep-learning networks, we

made images into $31 \times 31 \times 31$ patches with stride 15. More than 4300 patches were made from the data of each subject, with more than 12,900 patches in total made for the training set. This allowed large number of training patches to be generated with a small number of subjects, providing sufficient data for the deep-learning network training. For test, volume images were fed into the trained DPI-net as the input.

2.5 | Comparison with a single-stream network

To evaluate the effectiveness of DPI-net's multistream architecture, we compared DPI-net with a single-stream network. DPI-net has 32 multiple streams (the number of channels in MS-net); the single-stream network was designed to have a single stream in MS-net and to have a similar number of trainable parameters (500,257) as DPI-net (487,777). The only different parameter in the single-stream network was the number of feature maps of the convolution layers in MS-net ($c_{MS} = 32$); other parameters were the same as for DPI-net.

2.6 | Comparison with conventional methods

We compared DPI-net with the conventional PI methods, SAKE¹⁵ and ESPIRiT.¹⁶ These methods were developed to reconstruct 2D MR image, so we applied the methods to 2D multislice k-space data, made by the inverse Fourier transform of the original 3D k-space data along the readout direction. The parameters for the SAKE method were as follows: calibration region, 30×56 ; kernel size, 6×6 ; threshold of eigenvectors in k-space and image space, 0.02 and 0.09, respectively; and number of conjugate-gradient iterations, 100. The parameters for the ESPIRiT method were as follows: calibration region, 30×56 ; kernel size, 6×6 ; iterations, 100; window-normalized number of singular values to threshold, 1.8; and threshold of the eigenvectors in image space, 0.9.

To evaluate the effectiveness of DPI-net, we also compared it with U-net,³⁶ a conventional deep-learning method that has been widely used for undersampled MR image reconstruction.^{22,26} The original U-net was slightly modified to be effectively applicable to our data sets in this study. The number of feature maps of the first and final convolution layers were 32 and 1, respectively, and that of other convolution layers were half those of the original. There was batch normalization in each layer between the ReLU and convolution operations.

2.7 | Quantitative image analysis

The effectiveness of image reconstruction was evaluated using 3 objective measures: the normalized root mean square error (NRMSE), the peak SNR (PSNR), and

structural similarity (SSIM).³⁷ The visibility of the blood vessels was assessed by comparing the vessel sharpness, defined as the distance between locations at 20% and 80% of the maximum signal intensity of the vessel line profile.^{12,38} For an efficient comparison, we normalized the measured vessel sharpness by the value of the fully sampled image and took its inverse. Thus, larger values for vessel sharpness indicate sharper vessel edges. Five measured values for each vessel were averaged. Vessel line profiles were selected from middle cerebral arteries (MCAs) and posterior cerebral arteries (PCAs) on axial MIP image.

2.8 | Statistical analysis

Paired *t* tests³⁹ were used to compare the vessel sharpness between the reconstruction methods. *P* values <0.05 were considered statistically significant.

3 | RESULTS

3.1 | Multistream network versus single-stream network

Figure 2 shows fully sampled and reconstructed 3D TOF axial maximum intensity projection (MIP) images reconstructed by zero-filled, the single-stream network, and DPI-net, with the corresponding axial slices and magnified images, to evaluate the effectiveness of DPI-net's multistream architecture at the reduction factor $R = 5.7$. The zero-filled image shows that severe aliasing artifacts occurred, with several blood vessels obscured or not visible in the axial MIP image. The

single-stream network image shows recovery of many of the obscured blood vessels, although some blood vessels were not fully restored. The multistream network showed better performance in recovering the blood vessels in the axial MIP image and corresponding axial slice. The vessel signals obscured by aliasing artifacts in the zero-filled and single-stream network axial slice images were recovered in the multistream network image to a level similar to that in the fully sampled axial slice, thus resulting in a better axial MIP image than produced by the single-stream network. The quantitative metrics, including NRMSE and SSIM values, which are given at the top of the images, supported these observations. NRMSE values for the single-stream network and multistream network were lower than those for zero-filled in both the axial slices and MIP images, and the SSIM values were higher. Furthermore, there were improvements in NRMSE and SSIM values for the multistream network in the axial MIP images compared to the single-stream network; these improvements are more clearly presented in the axial slices, with much lower NRMSE and higher SSIM values than the single-stream network. The detailed comparison between the single-stream network and multistream network for the reduction factors $R = 5.7$ and 7.6 are presented in Supporting Information Table S1.

3.2 | DPI-net versus conventional methods

We compared DPI-net with the conventional methods SAKE, ESPIRiT, and U-net. Figure 3 shows fully sampled and reconstructed 3D TOF axial slices with magnified images and difference images produced by zero-filled, the 3 conventional

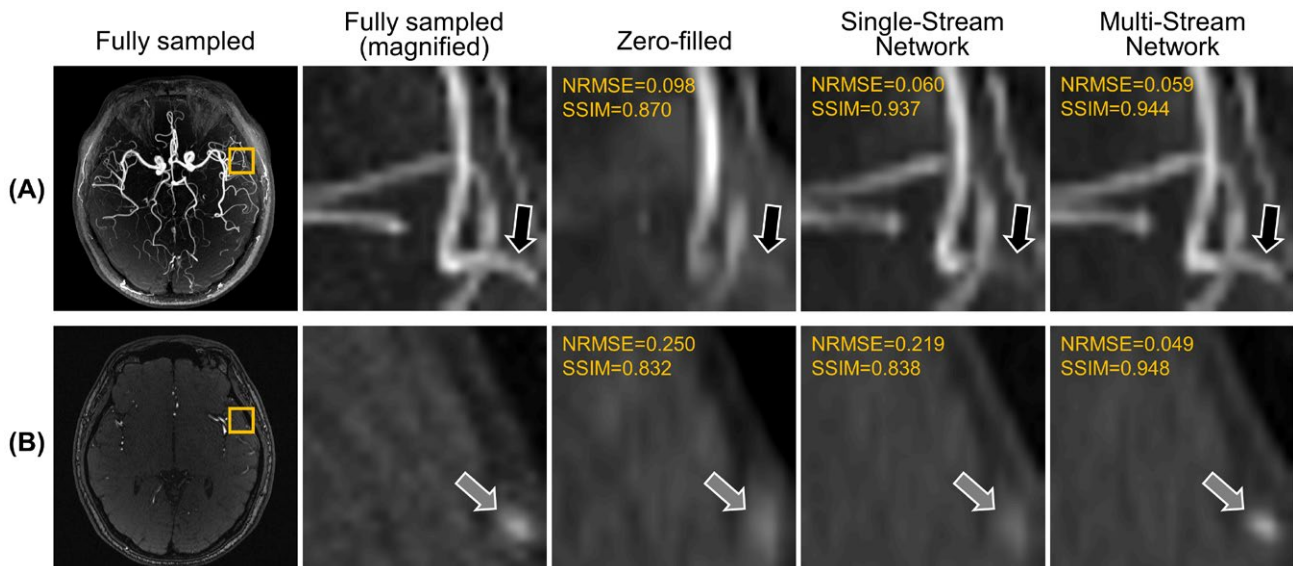


FIGURE 2 Reconstruction results for 3D TOF images reconstructed by fully sampled, zero-filled, a single-stream network, and a multistream network (DPI-net), with their magnified images, with the reduction factor $R = 5.7$. (A) Axial MIP images. (B) The corresponding axial slices. NRMSE and SSIM values are given at the top of the images. The black and gray arrows indicate vessel signals. As indicated by the arrows, DPI-net shows better performance in recovering the blood vessels than the single-stream network

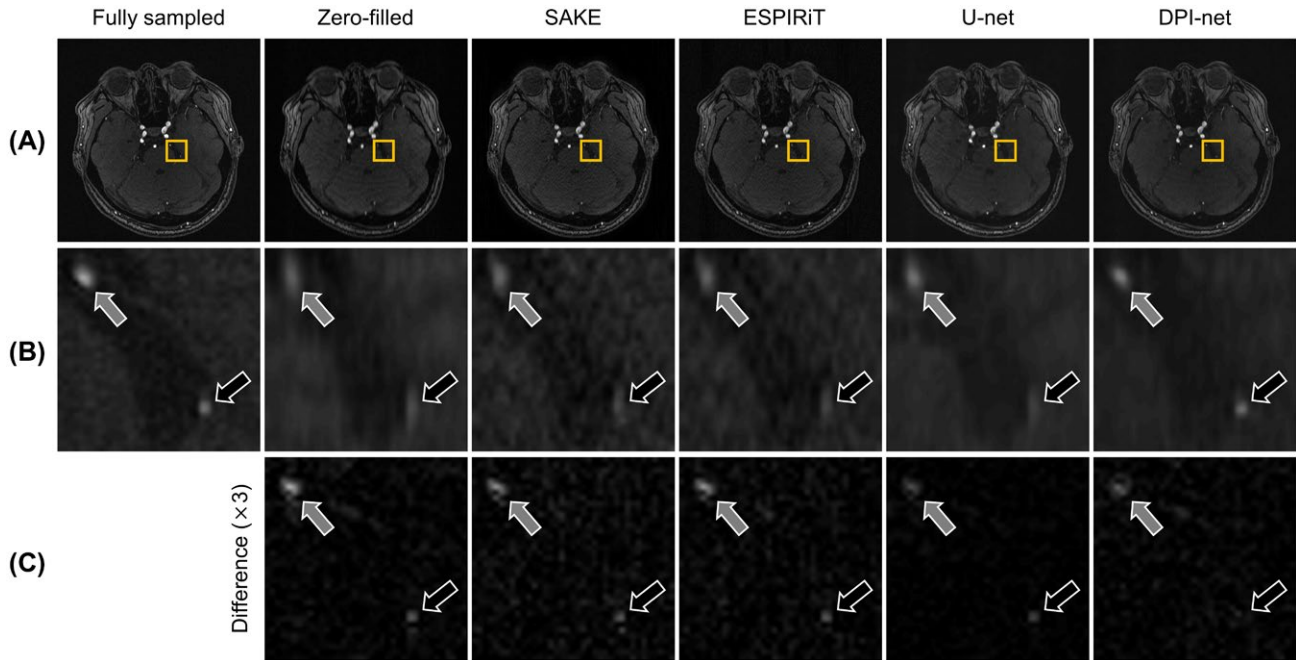


FIGURE 3 Reconstruction results for 3D TOF images reconstructed by fully sampled, zero-filled, SAKE, ESPIRiT, U-net, and DPI-net, with the reduction factor $R = 5.7$. (A) Axial slices. (B) Magnified images. (C) Difference images. The black and gray arrows indicate vessel signals. As indicated by the arrows, DPI-net shows better performance than the conventional methods in recovering the vessel signals

methods, and DPI-net, with a reduction factor $R = 5.7$. The zero-filled image showed aliasing artifacts that obscured vessel signals. The SAKE and ESPIRiT images showed fewer aliasing artifacts than the zero-filled image, but both images had high oscillatory noise and the obscured vessel signals were not fully restored, as can be seen in the difference images. In the U-net image, 1 vessel had a better restored signal than with the PI methods, but other vessel signals were not recovered. DPI-net showed better performance than the conventional methods in recovering the vessel signals and removing aliasing artifacts.

Axial, sagittal, and coronal MIP images, fully sampled and reconstructed by the various methods with the reduction factor $R = 5.7$, are shown in Figures 4, 5, and 6, respectively. In the axial MIP images, the 3 conventional methods could not restore one of anterior cerebral artery segments, which was not visible in zero-filled image because of aliasing artifacts, whereas DPI-net recovered the segment so that it was clearly visible as in the fully sampled image (Figure 4). In the sagittal MIP images, DPI-net restored vessel signals lost in the zero-filled image, unlike the other methods (Figure 5). In addition, several peripheral arteries were obscured in

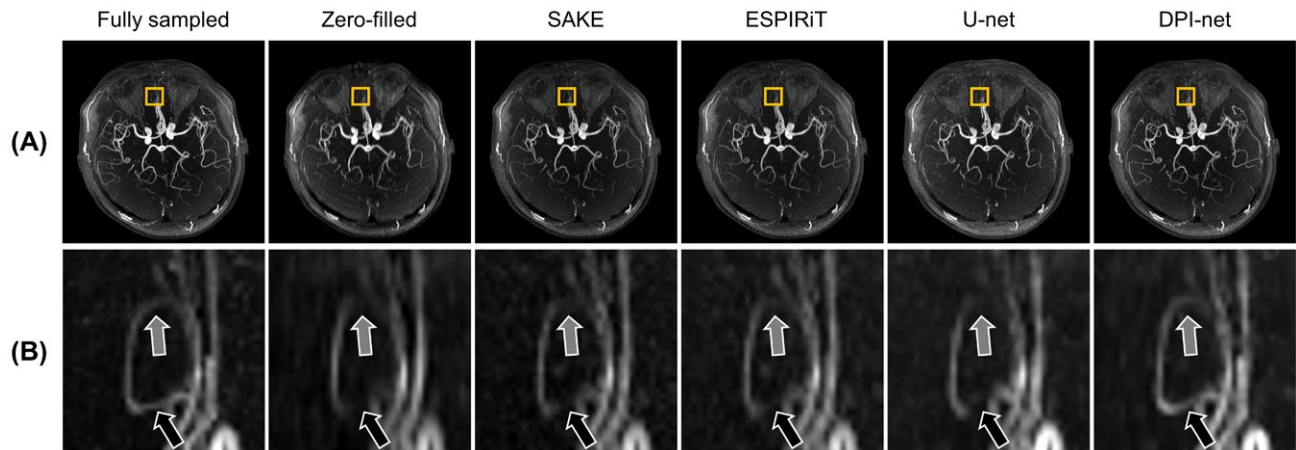


FIGURE 4 Reconstruction results for 3D TOF images reconstructed by fully sampled, zero-filled, SAKE, ESPIRiT, U-net, and DPI-net, with the reduction factor $R = 5.7$. (A) Axial MIP images. (B) Magnified images. The black and gray arrows indicate anterior cerebral artery segments. The black arrows show that SAKE, ESPIRiT, and U-net hardly restore the segment, whereas DPI-net recovers it

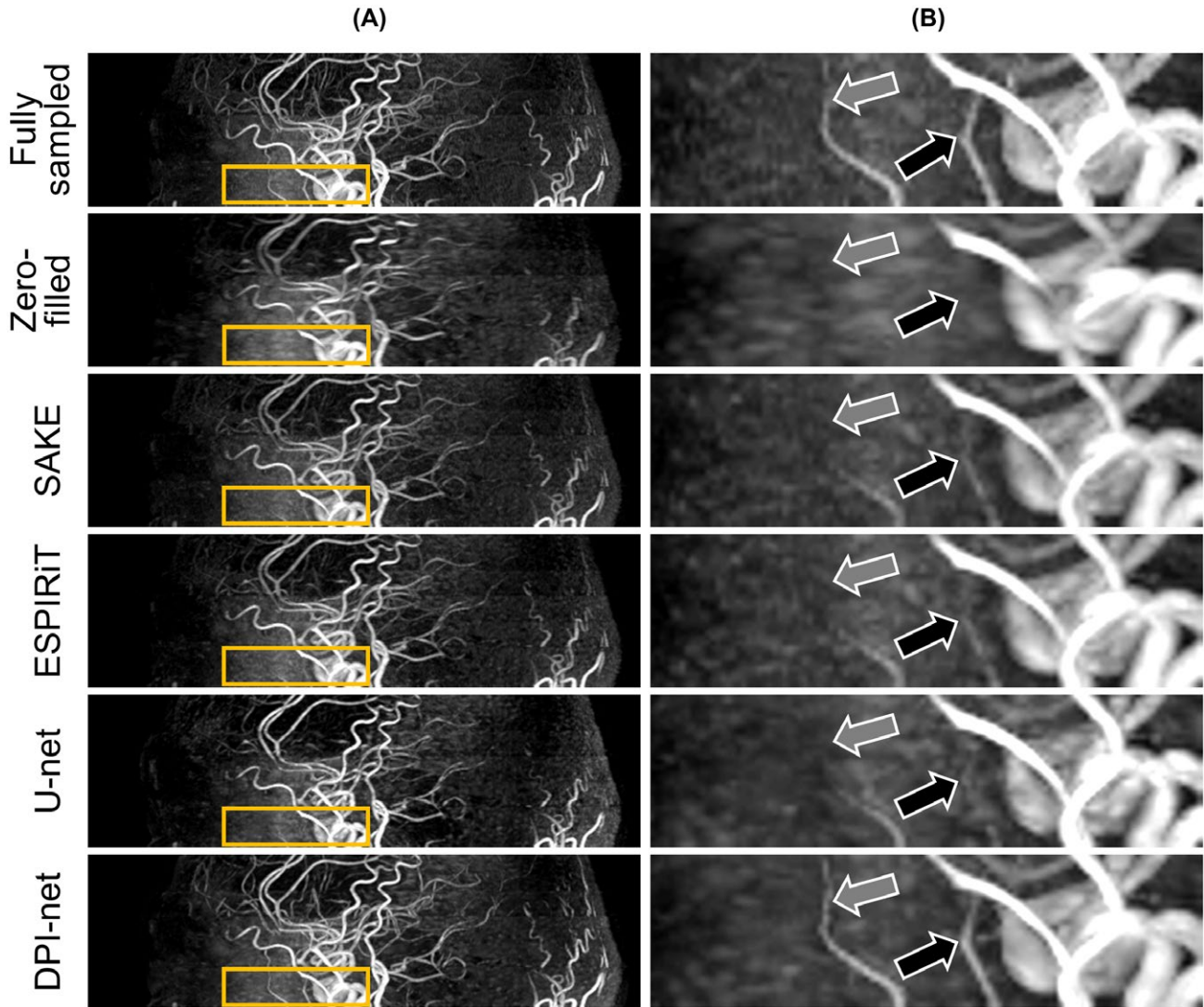


FIGURE 5 Reconstruction results for 3D TOF images reconstructed by fully sampled, zero-filled, SAKE, ESPIRiT, U-net, and DPI-net, with the reduction factor $R = 5.7$. (A) Sagittal MIP images. (B) Magnified images. The black and gray arrows indicate blood vessels. As indicated by the arrows, DPI-net shows better performance than the conventional methods in recovering the vessel signals

sagittal MIP images reconstructed by the conventional methods. In contrast, DPI-net showed peripheral arteries as clearly as those in the fully sampled. Similar results were observed with the coronal MIP images (Figure 6). The magnified images showed that thin blood vessels were hardly recovered by SAKE and ESPIRiT methods. The performance of U-net was degraded, with a low SNR where severe noise-like artifacts occurred in the overall coronal MIP images, whereas DPI-net clearly recovered the thin blood vessels. Axial, sagittal, and coronal MIP images for the reduction factor $R = 3.8$ are presented in Supporting Information Figures S2, S3, and S4, respectively, and those for the reduction factor $R = 7.6$ are presented in Supporting Information Figures S5, S6, and S7.

Table 1 presents the NRMSE, PSNR, and SSIM values for axial slices and axial, sagittal, and coronal MIP images for the reduction factors, $R = 3.8$, 5.7 , and 7.6 . With $R = 3.8$, DPI-net showed the lowest NRMSE and the highest PSNR

and SSIM values in the axial slices and axial and coronal MIP images; however, in the sagittal MIP images, ESPIRiT showed slightly better performance than DPI-net in terms of PSNR and SSIM values. For $R = 5.7$, DPI-net showed the lowest NRMSE and the highest PSNR and SSIM values for all except 2 cases, where U-net and ESPIRiT had slightly higher SSIM values in the axial slices and sagittal MIP images, respectively. For $R = 7.6$, DPI-net outperformed the conventional methods in all cases in the values of NRMSE, PSNR, and SSIM.

Figure 7 and Table 2 show the comparison of vessel sharpness for 4 vessels (right MCA, left MCA, right PCA, and left PCA) between the different reconstruction methods with the reduction factor $R = 5.7$. For the right MCA, DPI-net showed higher vessel sharpness than the 4 other methods. The same was the case for the left MCA, and for the left PCA. For the right PCA, DPI-net showed higher vessel sharpness

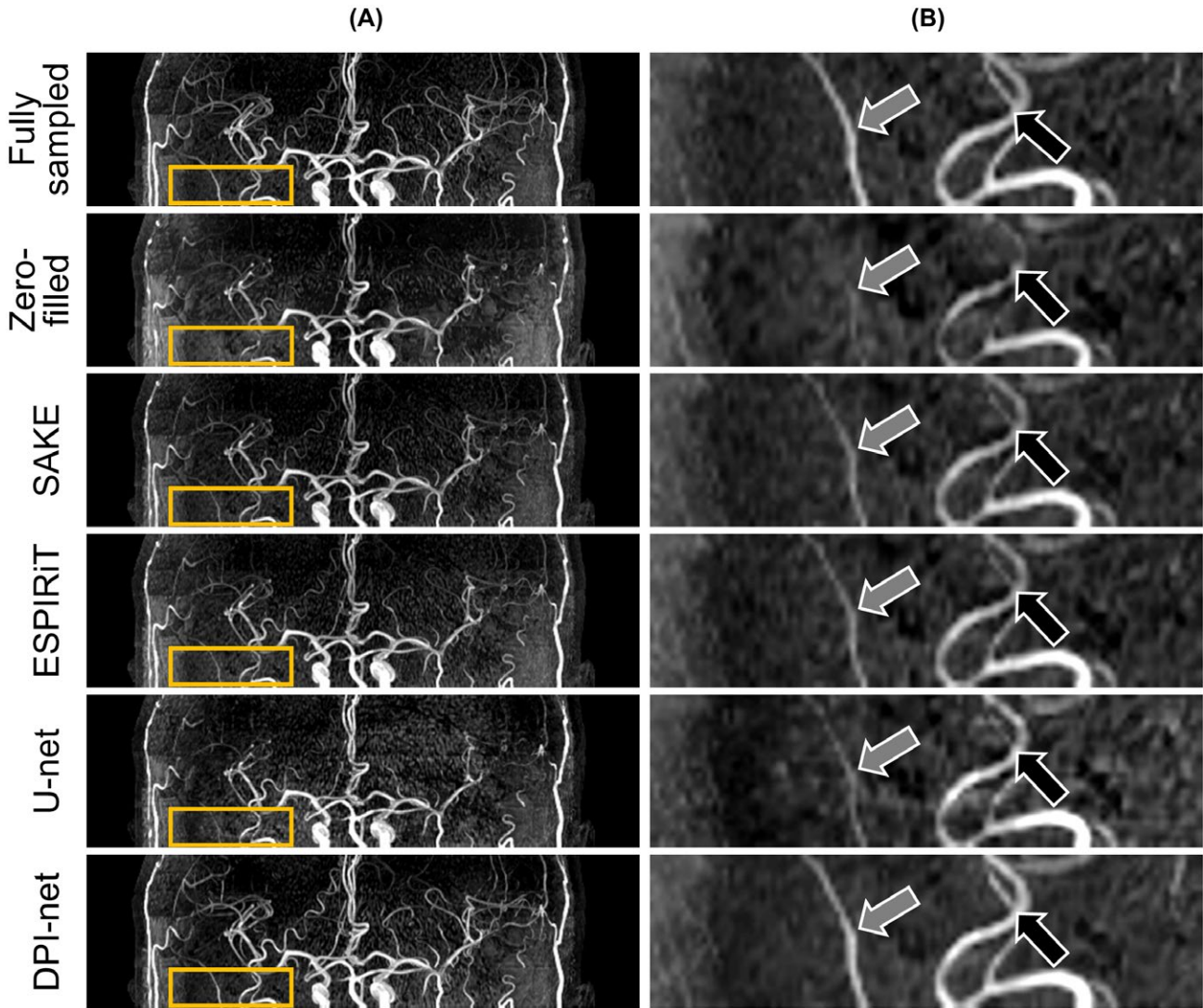


FIGURE 6 Reconstruction results for 3D TOF images reconstructed by fully sampled, zero-filled, SAKE, ESPIRiT, U-net, and DPI-net, with the reduction factor $R = 5.7$. (A) Coronal MIP images. (B) Magnified images. The black and gray arrows indicate blood vessels. The arrows show that SAKE, ESPIRiT, and U-net hardly restore blood vessels, whereas DPI-net recovers them

only compared with zero-filled. Overall, DPI-net showed significantly higher vessel sharpness than all the other reconstruction methods. To validate the performance of DPI-net for the various reduction factors, reconstructed sagittal slices, MIP images, and difference images with different reduction factors from the same subject are presented in Figure 8. For the reduction factor $R = 3.8$, most blood vessels (apart from some peripheral ones) were preserved; however, for high reduction factor $R = 7.6$, the errors increased, as shown in the difference images.

3.3 | Computation time comparison

We measured and compared the computation time of the 3D TOF MRA reconstruction methods. The original SAKE and ESPIRiT codes were designed to operate with a CPU using MATLAB software (The MathWorks, Inc., Natick, MA).^{15,16}

We measured their computation time with single Intel i7-6700K CPU, which has 8 cores in MATLAB software. The averaged computation times for SAKE and ESPIRiT for reconstructing the 3D volume image were 48 and 25 hours, respectively. U-net and DPI-net were designed to operate on a single Nvidia GeForce GTX 1080Ti GPU with a python *Tensorflow* library.³⁴ The averaged computation times of U-net and DPI-net for reconstructing the 3D volume image were 33 and 56 seconds, respectively.

4 | DISCUSSION

This study describes DPI-net, a new 3D PI method to reconstruct 3D TOF MRA from undersampled multichannel MR data using a deep-learning network. To the best of our knowledge, no previous deep-learning-based studies have

TABLE 1 Comparison between the reconstruction methods of the evaluation results for 3D TOF MRA reconstruction (NRMSE/PSNR/SSIM) at 3 reduction factors

Data	Method	Reduction factor		
		R = 3.8	R = 5.7	R = 7.6
Axial slices	Zero-filled	0.031/30.56/0.884	0.051/26.32/0.830	0.081/22.29/0.755
	SAKE	0.034/29.61/0.670	0.040/28.22/0.644	0.053/25.81/0.616
	ESPIRiT	0.032/30.08/0.795	0.039/28.49/0.774	0.055/25.61/0.722
	U-net	0.017/35.50/0.892	0.024/32.72/ 0.861	0.033/30.11/0.826
	DPI-net	0.016/35.87/0.898	0.022/33.20/0.860	0.024/32.63/0.850
Axial MIP	Zero-filled	0.026/31.98/0.898	0.035/29.34/0.836	0.047/26.91/0.743
	SAKE	0.032/30.11/0.837	0.035/29.43/0.818	0.039/28.45/0.775
	ESPIRiT	0.018/35.10/0.807	0.022/33.35/0.780	0.030/30.80/0.719
	U-net	0.019/35.00/0.899	0.026/31.91/0.848	0.035/29.45/0.837
	DPI-net	0.017/35.90/0.914	0.021/33.82/0.893	0.026/32.06/0.857
Sagittal MIP	Zero-filled	0.038/28.64/0.824	0.053/25.78/0.729	0.069/23.45/0.624
	SAKE	0.025/32.41/0.881	0.032/30.25/0.839	0.043/27.56/0.762
	ESPIRiT	0.024/32.77/0.898	0.032/30.31/ 0.853	0.044/27.38/0.767
	U-net	0.026/32.02/0.874	0.041/28.08/0.774	0.054/25.56/0.666
	DPI-net	0.024/32.68/0.895	0.030/30.66/0.851	0.039/28.36/0.790
Coronal MIP	Zero-filled	0.036/29.12/0.869	0.050/26.37/0.785	0.064/24.21/0.691
	SAKE	0.025/32.19/0.905	0.033/30.01/0.872	0.044/27.43/0.805
	ESPIRiT	0.023/32.88/0.917	0.032/30.32/0.881	0.044/27.38/0.809
	U-net	0.025/32.42/0.902	0.043/27.73/0.806	0.054/25.69/0.702
	DPI-net	0.023/33.06/0.921	0.029/30.97/0.889	0.039/28.58/0.836

The lowest NRMSE and highest PSNR and SSIM values are in bold font.

TABLE 2 Comparison of vessel sharpness for different vessels between different reconstruction methods with the reduction factor R = 5.7

Method	Vessels				
	All	Right MCA	Left MCA	Right PCA	Left PCA
Zero-filled	0.828 ^{***}	0.862 ^{***}	0.688 ^{***}	0.995 [*]	0.766 ^{***}
SAKE	1.024 ^{***}	1.062 [*]	0.881 [*]	1.176	0.975 [*]
ESPIRiT	0.988 ^{***}	1.052 ^{**}	0.882 [*]	1.130	0.888 ^{**}
U-net	1.014 ^{***}	1.119 [*]	0.799 ^{**}	1.167	0.971 [*]
DPI-net	1.251	1.397	1.192	1.294	1.120

The highest vessel sharpness values are in bold font. Paired *t* tests were used to calculate *P* values. ^{*}*P* < 0.05; ^{**}*P* < 0.01; ^{***}*P* < 0.001.

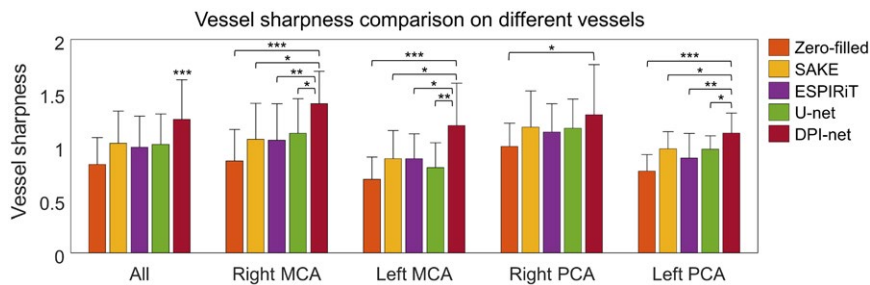


FIGURE 7 Vessel sharpness comparison on 4 different vessels (right MCA, left MCA, right PCA, and left PCA) with different reconstruction methods including zero-filled, SAKE, ESPIRiT, U-net, and DPI-net with the reduction factor R = 5.7. Paired *t* tests were used to calculate *P* values. ^{*}*P* < 0.05; ^{**}*P* < 0.01; ^{***}*P* < 0.001

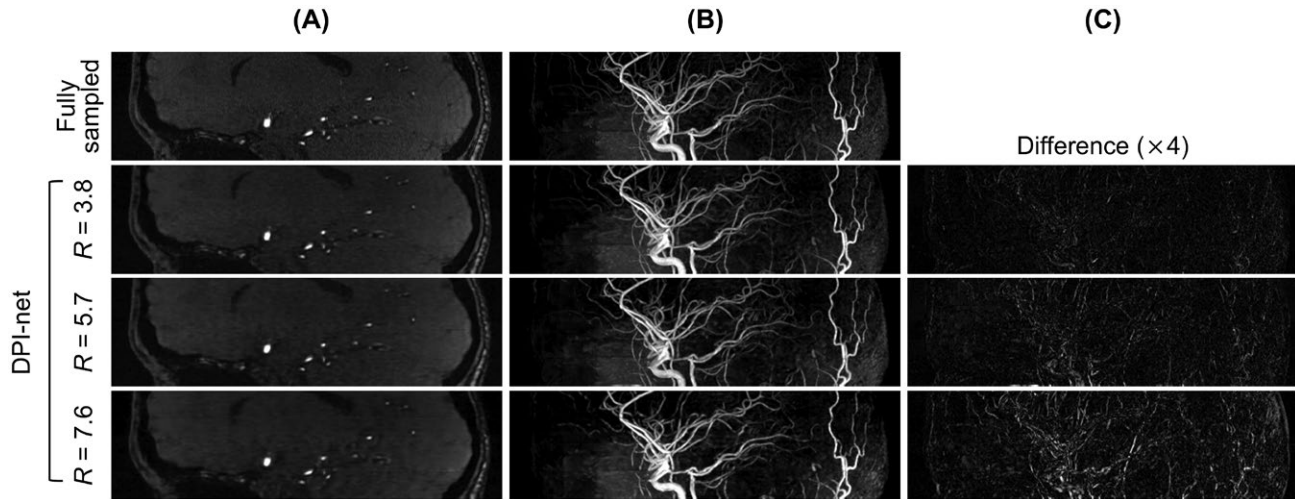


FIGURE 8 Reconstruction results for 3D TOF images by DPI-net, with the reduction factors $R = 3.8, 5.7,$ and 7.6 . (A) Sagittal slices. (B) Sagittal MIP images. (C) Difference images of sagittal MIP images

reconstructed 3D TOF MRA from undersampled multichannel MR data. DPI-net comprises 2 deep-learning networks: MS-net and RC-net. MS-net extracts feature maps of multichannel MR images using multistream CNNs and RC-net reconstructs the images from the MS-net output feature maps. Through qualitative and quantitative analyses, we demonstrated that DPI-net outperformed the conventional PI methods SAKE and ESPIRiT, as well as a widely used deep-learning-based method, U-net, in reconstructing 3D TOF MRA for high reduction factors. In particular, DPI-net showed superior performance compared to the other methods in restoring vessel signals lost in undersampled axial slices and MIP images, producing blood vessels in images as clearly as those from fully sampled. In addition, DPI-net reconstructed 3D TOF MRA more quickly than the conventional PI methods. The computation time of most of PI methods increases by as much as the third order of the number of coils.⁴⁰ Most of the computation times in SAKE and ESPIRiT were spent in performing singular value decomposition on large data matrix with several iterations.^{15,16} In 3D TOF MRA, computation by SAKE and ESPIRiT took more than a day, which meant these methods were not feasible for online reconstruction. For DPI-net, it required extensive time for training, which took approximately 48 hours with a single GPU; however, once the training of DPI-net is finished, it does not require additional optimization or parameter selection. Applying the trained DPI-net to test data is relatively fast, which took less than 1 minute for reconstruction, making it suitable for online reconstruction. Furthermore, for the fair comparison with the conventional PI methods, SAKE and ESPIRiT, we measured the computation time of DPI-net operating on CPU. The averaged computation time of DPI-net with CPU was 29 minutes, which was still faster than SAKE and ESPIRiT.

Our objective function is formulated as Equation 4 where the SSOS of the fully sampled multichannel 3D MR images is

the desired output and magnitude of the undersampled multichannel 3D MR images is the input. The phase information of the multichannel images has not been used for the input of DPI-net. To validate the case where the phase information is preserved, we performed an experiment by including the real and imaginary components of the multichannel images as separate channels for the input of DPI-net. Supporting Information Figure S8 shows that adding phase information did not improve the performance in recovering the vessel signals and removing aliasing artifacts. One study has been proposed that the magnitude network, which was trained with magnitude input, showed better performance than the complex network, which was trained with 2 channels of real and imaginary components.⁴¹ In our case, the 3D TOF MRA does not require phase information in MIP images. Thus, we used the magnitude of the undersampled multichannel 3D MR images for the input of DPI-net.

Our evaluation demonstrated the effectiveness of DPI-net's multistream network architecture compared to a single-stream network. The conventional single-stream network required more parameters to extract the features of the multichannel data. In this case, it required slightly more trainable parameters (500,277) than the multistream network (487,777); however, the multistream network showed better performance than the single-stream in restoring vessel signals. Multistream networks are also known as multibranch, multipath, and split-transform-merge networks.⁴² Various types of multistream network have been proposed to simultaneously improve the performance and reduce the complexity of a deep-learning network.⁴² The well-known deep-learning architectures, Inception-network⁴³ and ResNets,²⁹ are examples of multistream or multibranch networks.⁴² To extract features from a large MR data set, such as multichannel 3D TOF MRA, required designing deep-learning architecture with low computational complexity and improved performance.

We therefore introduced MS-net, a network of multistream CNNs, to extract features from the multichannel 3D TOF MRA data effectively before feeding the data into the reconstruction network.

For further validation of MS-net, we changed the input feature maps of RC-net with 3 different ones and compared their results: the output of coil compression algorithm,^{40,44} features of shared MS-net, which shared convolution weights across different branches, and features of the original MS-net (Supporting Information Figure S9). We used the coil compression algorithm proposed by Zhang et al⁴⁴ and compressed 32 coils into 8 virtual coils. When the input of RC-net was the original MS-net feature maps, it showed superior performance compared to the other methods in restoring vessel signals. The performance of coil compression with RC-net was degraded compared to MS-net with RC-net, suggesting that the coil compression algorithm could not represent MS-net.

Recently, several studies have been proposed for single-coil MR image reconstruction from undersampled k-space data using CNNs. We additionally compared DPI-net with generative adversarial neural networks for compressive sensing (GANCS)⁴⁵ and deep cascade CNNs,⁴⁶ but we found that expansion of them to PI methods was beyond the scope of this study. Thus, we implemented GANCS and deep cascade CNNs in each coil individually and combined their reconstruction results. DPI-net showed superior performance in reconstructing vessel signals in MIP images (Supporting Information Figure S10). This was supported by the quantitative metrics, with DPI-net showing the lowest NRMSE, and the highest PSNR and SSIM values for all except 1 case, where deep cascade CNNs had slightly higher PSNR values in the axial slices for $R = 5.7$ (Supporting Information Table S2). Furthermore, DPI-net showed significantly higher vessel sharpness values than the other methods (Supporting Information Table S3).

Computing large MR data, such as multichannel 3D MR data, on a single personal computer can result in issues of insufficient RAM or GPU memory. To handle large 3D TOF MRA data sets, we used swap memory in addition to the RAM and adjusted the minibatch size to train the deep-learning network with a single GPU. Another possible way to deal with large MR data sets is to reduce their size; this can be achieved using the coil compression algorithm, which compresses multiple coils into a smaller number of virtual coils.^{40,44} Compressing the number of coils would reduce the number of extracting features required for the MS-net, thereby reducing the size of the data set and potentially enabling faster training and inference of DPI-net.

The training of DPI-net with multichannel 3D MRA requires lots of training data and computation memory. For efficient and effective training of DPI-net, we made the input and output images into $31 \times 31 \times 31$ patches. This allowed a large number of training patches to be generated with a small

number of subjects, providing sufficient data for the deep-learning network training. In contrast, for test of DPI-net, volume images were fed into the trained DPI-net as the input, which is not a patch-based procedure. This test procedure is the same as common image-based CNNs, which can preserve the entire image structure and avoid hallucination.¹⁸ These training and test procedures are a well-known deep-learning scheme for image super-resolution, denoising, and artifact reduction.^{18,20,21,47} Several studies have been proposed in MR image reconstruction using the same deep-learning scheme,^{25,48,49} but they did not report a hallucination problem in the training or test.

The 3D TOF MRA data for the present study were acquired from healthy subjects with no vascular-related diseases. In future work, we will validate DPI-net using pathological cases, such as patients with vascular-related diseases (e.g., intracranial vascular aneurysms, stenosis, and occlusion). Furthermore, because DPI-net is designed to handle 4D data (3D data with multiple channels), our future work will include applying it to various MR data reconstructions that require high dimensionality, such as 3D turbo-spin-echo sequences for whole-brain scans, dynamic sequences for cardiac imaging, and functional MRI sequences for measuring functional brain connectivity.

ACKNOWLEDGMENTS

This research was supported by the National Research Foundation of Korea (NRF) grant funded by the Korean government (MSIP; 2016R1A2B4015016) and National Research Foundation of Korea (NRF) grant funded by the Korean government (MSIT; 2018M3C7A1024734).

ORCID

Yohan Jun  <https://orcid.org/0000-0003-4787-4760>

Ho-Joon Lee  <https://orcid.org/0000-0003-0831-6184>

REFERENCES

1. Graves M. Magnetic resonance angiography. *Br J Radiol.* 1997;70:6–28.
2. Dagirmanjian A, Ross JS, Obuchowski N, et al. High resolution, magnetization transfer saturation, variable flip angle, time-of-flight MRA in the detection of intracranial vascular stenoses. *J Comput Assist Tomogr.* 1995;19:700–706.
3. Oelerich M, Lentschig M, Zunker P, Reimer P, Rummeny E, Schuierer G. Intracranial vascular stenosis and occlusion: comparison of 3D time-of-flight and 3D phase-contrast MR angiography. *Neuroradiology.* 1998;40:567–573.
4. White PM, Wardlaw JM, Easton V. Can noninvasive imaging accurately depict intracranial aneurysms? A systematic review. *Radiology.* 2000;217:361–370.

5. White PM, Teasdale EM, Wardlaw JM, Easton V. Intracranial aneurysms: CT angiography and MR angiography for detection—prospective blinded comparison in a large patient cohort. *Radiology*. 2001;219:739–749.
6. Gibbs GF, Huston J, Bernstein MA, Riederer SJ, Brown RD. Improved image quality of intracranial aneurysms: 3.0-T versus 1.5-T time-of-flight MR angiography. *Am J Neuroradiol*. 2004;25:84–87.
7. Weber J, Veith P, Jung B, et al. MR angiography at 3 Tesla to assess proximal internal carotid artery stenoses: contrast-enhanced or 3D time-of-flight MR angiography? *Clin Neuroradiol*. 2015;25:41–48.
8. Wilson GJ, Hoogeveen RM, Willinek WA, Muthupillai R, Maki JH. Parallel imaging in MR angiography. *Top Magn Reson Imaging*. 2004;15:169–185.
9. Lustig M, Donoho D, Pauly JM. Sparse MRI: The application of compressed sensing for rapid MR imaging. *Magn Reson Med*. 2007;58:1182–1195.
10. Lustig M, Donoho DL, Santos JM, Pauly JM. Compressed sensing MRI. *IEEE Signal Process Mag*. 2008;25:72–82.
11. Yamamoto T, Fujimoto K, Okada T, et al. Time-of-flight magnetic resonance angiography with sparse undersampling and iterative reconstruction: comparison with conventional parallel imaging for accelerated imaging. *Invest Radiol*. 2016;51:372–378.
12. Fushimi Y, Fujimoto K, Okada T, et al. Compressed sensing 3-dimensional time-of-flight magnetic resonance angiography for cerebral aneurysms: optimization and evaluation. *Invest Radiol*. 2016;51:228–235.
13. Pruessmann KP, Weiger M, Scheidegger MB, Boesiger P. SENSE: sensitivity encoding for fast MRI. *Magn Reson Med*. 1999;42:952–962.
14. Griswold MA, Jakob PM, Heidemann RM, et al. Generalized autocalibrating partially parallel acquisitions (GRAPPA). *Magn Reson Med*. 2002;47:1202–1210.
15. Shin PJ, Larson PE, Ohliger MA, et al. Calibrationless parallel imaging reconstruction based on structured low-rank matrix completion. *Magn Reson Med*. 2014;72:959–970.
16. Uecker M, Lai P, Murphy MJ, et al. ESPIRiT—an eigenvalue approach to autocalibrating parallel MRI: where SENSE meets GRAPPA. *Magn Reson Med*. 2014;71:990–1001.
17. Murphy M, Alley M, Demmel J, Keutzer K, Vasanawala S, Lustig M. Fast l_1 SPIRiT compressed sensing parallel imaging MRI: scalable parallel implementation and clinically feasible runtime. *IEEE Trans Med Imaging*. 2012;31:1250–1262.
18. Dong C, Loy CC, He K, Tang X. Image super-resolution using deep convolutional networks. *IEEE Trans Pattern Anal Mach Intell*. 2016;38:295–307.
19. Xie J, Xu L, Chen E. Image denoising and inpainting with deep neural networks. In Proceedings of the Advances in Neural Information Processing Systems, Stateline, NV, 2012. pp. 341–349.
20. Kim J, Kwon Lee J, Mu Lee K. Accurate image super-resolution using very deep convolutional networks. In Proceedings of the IEEE Conference on Computer Vision and Pattern Recognition, Las Vegas, NV, 2016. pp. 1646–1654.
21. Zhang K, Zuo W, Chen Y, Meng D, Zhang L. Beyond a gaussian denoiser: Residual learning of deep cnn for image denoising. *IEEE Trans Image Process*. 2017;26:3142–3155.
22. Yang G, Yu S, Dong H, et al. Dagan: Deep de-aliasing generative adversarial networks for fast compressed sensing MRI reconstruction. *IEEE Trans Med Imaging*. 2018;37:1310–1321.
23. Kwon K, Kim D, Park H. A parallel MR imaging method using multilayer perceptron. *Med Phys*. 2017;44:6209–6224.
24. Hammernik K, Klatzer T, Kobler E, et al. Learning a variational network for reconstruction of accelerated MRI data. *Magn Reson Med*. 2018;79:3055–3071.
25. Eo T, Jun Y, Kim T, Jang J, Lee HJ, Hwang D. KIKI-net: cross-domain convolutional neural networks for reconstructing undersampled magnetic resonance images. *Magn Reson Med*. 2018;80:2188–2201.
26. Hyun CM, Kim HP, Lee SM, Lee S, Seo JK. Deep learning for undersampled MRI reconstruction. *Phys Med Biol*. 2018;63:135007.
27. Eitel A, Springenberg JT, Spinello L, Riedmiller M, Burgard W. Multimodal deep learning for robust rgb-d object recognition. In Proceedings of the Intelligent Robots and Systems, Hamburg, Germany, 2015. pp. 681–687.
28. Cheng D, Gong Y, Zhou S, Wang J, Zheng N. Person re-identification by multi-channel parts-based cnn with improved triplet loss function. In Proceedings of the IEEE Conference on Computer Vision and Pattern Recognition, Las Vegas, NV, 2016. pp. 1335–1344.
29. He K, Zhang X, Ren S, Sun J. Deep residual learning for image recognition. In Proceedings of the IEEE Conference on Computer Vision and Pattern Recognition, Las Vegas, NV, 2016. pp. 770–778.
30. Ioffe S, Szegedy C. Batch normalization: accelerating deep network training by reducing internal covariate shift. In Proceedings of the International Conference on Machine Learning, Lille, France, 2015. pp. 448–456.
31. Nair V, Hinton GE. Rectified linear units improve restricted boltzmann machines. In Proceedings of the International Conference on Machine Learning, Haifa, Israel, 2010. pp. 807–814.
32. He K, Zhang X, Ren S, Sun J. Delving deep into rectifiers: Surpassing human-level performance on imagenet classification. In Proceedings of the IEEE International Conference on Computer Vision, Santiago, Chile, 2015. pp. 1026–1034.
33. Kinga D, Adam JB. A method for stochastic optimization. In Proceedings of the International Conference on Learning Representations, San Diego, CA, 2015.
34. Abadi M, Barham P, Chen J, et al. Tensorflow: a system for large-scale machine learning. In Proceedings of the USENIX Symposium on Operating Systems Design and Implementation, Savannah, GA, 2016. pp. 265–283.
35. Vasanawala S, Murphy M, Alley MT, et al. Practical parallel imaging compressed sensing MRI: Summary of two years of experience in accelerating body MRI of pediatric patients. In Proceedings of the IEEE International Symposium on Biomedical Imaging, Chicago, IL, 2011. pp. 1039–1043.
36. Ronneberger O, Fischer P, Brox T. U-net: Convolutional networks for biomedical image segmentation. In Proceedings of the International Conference on Medical Image Computing and Computer-Assisted Intervention, Munich, Germany, 2015. pp. 234–241.
37. Wang Z, Bovik AC, Sheikh HR, Simoncelli EP. Image quality assessment: from error visibility to structural similarity. *IEEE Trans Image Process*. 2004;13:600–612.
38. Kramer JH, Arnoldi E, François CJ, et al. Dynamic and static magnetic resonance angiography of the supra-aortic vessels at 3.0 T: intraindividual comparison of gadobutrol, gadobenate dimeglumine, and gadoterate meglumine at equimolar dose. *Invest Radiol*. 2013;48:121–128.
39. McDonald JH. *Handbook of biological statistics*. Baltimore, MD: Sparky House; 2009.
40. Zhang T, Chowdhury S, Lustig M, et al. Clinical performance of contrast enhanced abdominal pediatric MRI with fast combined

parallel imaging compressed sensing reconstruction. *J Magn Reson Imaging*. 2014;40:13–25.

41. Lee D, Yoo J, Tak S, Ye JC. Deep residual learning for accelerated MRI using magnitude and phase networks. *IEEE Trans Biomed Eng*. 2018;65:1985–1995.
42. Xie S, Girshick R, Dollár P, Tu Z, He K. Aggregated residual transformations for deep neural networks. In Proceedings of the IEEE International Conference on Computer Vision, Venice, Italy, 2017. pp. 5987–5995.
43. Szegedy C, Ioffe S, Vanhoucke V, Alemi AA. Inception-v4, inception-resnet and the impact of residual connections on learning. In Proceedings of the Association for the Advancement of Artificial Intelligence, San Francisco, CA, 2017. p. 12.
44. Zhang T, Pauly JM, Vasanaawala SS, Lustig M. Coil compression for accelerated imaging with Cartesian sampling. *Magn Reson Med*. 2013;69:571–582.
45. Mardani M, Gong E, Cheng JY, et al. Deep Generative Adversarial Neural Networks for Compressive Sensing (GANCS) MRI. *IEEE Trans Med Imaging*. 2018 Jul 23. doi: <https://doi.org/10.1109/TMI.2018.2858752>. [Epub ahead of print]
46. Schlemper J, Caballero J, Hajnal JV, Price AN, Rueckert D. A deep cascade of convolutional neural networks for dynamic MR image reconstruction. *IEEE Trans Med Imaging*. 2018;37:491–503.
47. Dong C, Deng Y, Loy CC, Tang X. Compression artifacts reduction by a deep convolutional network. In Proceedings of the IEEE International Conference on Computer Vision, Santiago, Chile, 2015. pp. 576–584.
48. Wang S, Su Z, Ying L, et al. Accelerating magnetic resonance imaging via deep learning. In Proceedings of the IEEE International Symposium on Biomedical Imaging, Prague, Czech Republic, 2016. pp. 514–517.
49. Chaudhari AS, Fang Z, Kogan F, et al. Super-resolution musculoskeletal MRI using deep learning. *Magn Reson Med*. 2018;80:2139–2154.

SUPPORTING INFORMATION

Additional supporting information may be found online in the Supporting Information section at the end of the article.

FIGURE S1 Binary undersampling masks used in this study for the reduction factors $R = 3.8$, $R = 5.7$, and $R = 7.6$

FIGURE S2 Reconstruction results for 3D TOF images reconstructed by fully sampled, zero-filled, SAKE, ESPIRiT, U-net, and DPI-net, with the reduction factor $R = 3.8$. (a) Axial MIP images. (b) Magnified images

FIGURE S3 Reconstruction results for 3D TOF images reconstructed by fully sampled, zero-filled, SAKE, ESPIRiT, U-net, and DPI-net, with the reduction factor $R = 3.8$. (a) Sagittal MIP images. (b) Magnified images

FIGURE S4 Reconstruction results for 3D TOF images reconstructed by fully sampled, zero-filled, SAKE, ESPIRiT, U-net, and DPI-net, with the reduction factor $R = 3.8$. (a) Coronal MIP images. (b) Magnified images

FIGURE S5 Reconstruction results for 3D TOF images reconstructed by fully sampled, zero-filled, SAKE, ESPIRiT,

U-net, and DPI-net, with the reduction factor $R = 7.6$. (a) Axial MIP images. (b) Magnified images

FIGURE S6 Reconstruction results for 3D TOF images reconstructed by fully sampled, zero-filled, SAKE, ESPIRiT, U-net, and DPI-net, with the reduction factor $R = 7.6$. (a) Sagittal MIP images. (b) Magnified images

FIGURE S7 Reconstruction results for 3D TOF images reconstructed by fully sampled, zero-filled, SAKE, ESPIRiT, U-net, and DPI-net, with the reduction factor $R = 7.6$. (a) Coronal MIP images. (b) Magnified images

FIGURE S8 Reconstruction results for 3D TOF images reconstructed by fully sampled, zero-filled, DPI-net with magnitude and phase input, and DPI-net with magnitude input, with their magnified images, with the reduction factor $R = 5.7$. (a) Axial MIP images. (b) The corresponding axial slices. NRMSE and SSIM values are given at the bottom of the images. As indicated by the arrows, DPI-net with magnitude input shows better performance in recovering the blood vessels and removing aliasing artifacts than DPI-net with magnitude and phase input

FIGURE S9 Reconstruction results for 3D TOF images reconstructed by fully sampled, zero-filled, coil compression with RC-net, shared MS-net with RC-net, and DPI-net, with their magnified images, with the reduction factor $R = 5.7$. (a) Axial MIP images. (b,c) Corresponding axial slices of axial MIP images indicated by the black and gray arrows, respectively. NRMSE and SSIM values are given at the top of the images. As indicated by the arrows, DPI-net shows better performance in recovering blood vessels than the coil compression with RC-net and shared MS-net with RC-net

FIGURE S10 Reconstruction results for 3D TOF images reconstructed by fully sampled, zero-filled, GANCS, deep cascade CNNs, and DPI-net, with the reduction factor $R = 5.7$. (a) Sagittal MIP images. (b) Magnified images

TABLE S1 Comparison between the multistream network and single-stream network of the evaluation results for 3D TOF MRA reconstruction (NRMSE/PSNR/SSIM) at 2 reduction factors

TABLE S2 Comparison between the reconstruction methods of the evaluation results for 3D TOF MRA reconstruction (NRMSE/PSNR/SSIM) at 2 reduction factors

TABLE S3 Comparison of vessel sharpness for different vessels between different reconstruction method with the reduction factor $R = 5.7$

How to cite this article: Jun Y, Eo T, Shin H, Kim T, Lee H-J, Hwang D. Parallel imaging in time-of-flight magnetic resonance angiography using deep multistream convolutional neural networks. *Magn Reson Med*. 2019;00:1–14. <https://doi.org/10.1002/mrm.27656>